

# Precise and fast spatial-frequency analysis using the iterative local Fourier transform

SUKMOCK LEE,<sup>1</sup> HEEJOO CHOI,<sup>2</sup> AND DAE WOOK KIM<sup>2,\*</sup>

<sup>1</sup>Department of Physics, Inha University, Incheon, 402-751, South Korea

<sup>2</sup>College of Optical Sciences, University of Arizona, 1630 East University Boulevard, Tucson, Arizona 85721, USA

\*letter2dwk@hotmail.com

**Abstract:** The use of the discrete Fourier transform has decreased since the introduction of the fast Fourier transform (fFT), which is a numerically efficient computing process. This paper presents the iterative local Fourier transform (ilFT), a set of new processing algorithms that iteratively apply the discrete Fourier transform within a local and optimal frequency domain. The new technique achieves  $2^{10}$  times higher frequency resolution than the fFT within a comparable computation time. The method's superb computing efficiency, high resolution, spectrum zoom-in capability, and overall performance are evaluated and compared to other advanced high-resolution Fourier transform techniques, such as the fFT combined with several fitting methods. The effectiveness of the ilFT is demonstrated through the data analysis of a set of Talbot self-images ( $1280 \times 1024$  pixels) obtained with an experimental setup using grating in a diverging beam produced by a coherent point source.

©2016 Optical Society of America

**OCIS codes:** (300.6300) Spectroscopy, Fourier transforms; (070.4790) Spectrum analysis; (070.6760) Talbot and self-imaging effects.

## References and links

1. L. M. Sanchez-Brea, F. J. Torcal-Milla, J. M. Herrera-Fernandez, T. Morlanes, and E. Bernabeu, "Self-imaging technique for beam collimation," *Opt. Lett.* **39**(19), 5764–5767 (2014).
2. K. Patorski, M. Trusiak, and K. Pokorski, "Diffraction grating three-beam interferometry without self-imaging regime contrast modulations," *Opt. Lett.* **40**(6), 1089–1092 (2015).
3. K. Patorski, K. Pokorski, and M. Trusiak, "Circular-linear grating Talbot interferometry with moiré Fresnel imaging for beam collimation," *Opt. Lett.* **39**(2), 291–294 (2014).
4. S. De Nicola, P. Ferraro, G. Coppola, A. Finizio, G. Pierattini, and S. Grilli, "Talbot self-image effect in digital holography and its application to spectrometry," *Opt. Lett.* **29**(1), 104–106 (2004).
5. F. Pfeiffer, T. Weitkamp, O. Bunk, and C. David, "Phase retrieval and differential phase-contrast imaging with low-brilliance X-ray sources," *Nat. Phys.* **2**(4), 258–261 (2006).
6. J. Luo, J. Bai, J. Zhang, C. Hou, K. Wang, and X. Hou, "Long focal-length measurement using divergent beam and two gratings of different periods," *Opt. Express* **22**(23), 27921–27931 (2014).
7. C. van Loan, *Computational Frameworks for the Fast Fourier Transform* (SIAM, 1992).
8. G. Bachmann, L. Narici, and E. Beckenstein, *Fourier and wavelet analysis* (Springer Science & Business Media, 2012).
9. M. Frigo and S. G. Johnson, "FFTW: An adaptive software architecture for the FFT," *Acoustics, Speech and Signal Processing, 1998. Proceedings of the 1998 IEEE International Conference on Seattle, WA, (CSREA, 1998)*, pp. 1381–1384 vol.3.
10. A. Dutt and V. Rokhlin, "Fast Fourier transforms for nonequispaced data," *SIAM J. Sci. Comput.* **14**(6), 1368–1393 (1993).
11. J. R. Phillips and J. K. White, "A precorrected-FFT method for electrostatic analysis of complicated 3-D structures," *IEEE Trans. Comput. Aided Des. Integrated Circ. Syst.* **16**(10), 1059–1072 (1997).
12. J. Dongarra and F. Sullivan, "Guest Editors Introduction to the top 10 algorithms," *Comput. Sci. Eng.* **2**(1), 22–23 (2000).
13. J. S. Walker, *Fast Fourier transforms* (CRC, 1996), Vol. 24.
14. D. G. Voelz, *Computational Fourier Optics: A MATLAB® Tutorial* (SPIE, 2011).
15. M. Donadio, *Digital Signal Processing Articles*, "How to interpolate the peak location of a DFT or FFT if the frequency of interest is between bins." (1999) <http://dspguru.com/dsp/howtos/how-to-interpolate-fft-peak>.
16. J. P. Berrut and L. N. Trefethen, "Barycentric Lagrange interpolation," *SIAM Rev.* **46**(3), 501–517 (2004).
17. J. P. Berrut, R. Baltensperger, and H. D. Mittelmann, "Recent developments in barycentric rational interpolation." *Trends and applications in constructive approximation* (Birkhäuser Basel, 2005) 27–51.

18. Ta-Hsin Li and Kai-Sheng Song, "Estimation of the parameters of sinusoidal signals in non-Gaussian noise," *IEEE Transactions on Signal Processing*, (IEEE, **57**(1), 62–72 (2009).
19. J. Gai, F. Chan, Y. T. Chan, H. J. Du, and F. A. Dilkes, "Frequency Estimation of Uncooperative Coherent Pulse Radars," in *Proceedings of IEEE Conference on Military Communications* (IEEE, 1988), pp. 1–7.
20. J. Capon, "High-resolution frequency-wavenumber spectrum analysis," in *Proceedings of IEEE* (IEEE, 1969), **57**, pp. 1408–1418.
21. Wikipedia, "Discrete Fourier transform," [https://en.wikipedia.org/wiki/Discrete\\_Fourier\\_transform](https://en.wikipedia.org/wiki/Discrete_Fourier_transform).
22. Y. Nakano and K. Murata, "Talbot interferometry for measuring the focal length of a lens," *Appl. Opt.* **24**(19), 3162–3166 (1985).
23. A. Montaux-Lambert, P. Mercère, and J. Primot, "Interferogram conditioning for improved Fourier analysis and application to X-ray phase imaging by grating interferometry," *Opt. Express* **23**(22), 28479–28490 (2015).

## 1. Introduction

The Talbot self-image analysis [1–4] and Moiré pattern processing [5,6] are examples of data analysis methods that require the precise calculation of spatial frequency and the corresponding period. While some different types of frequency data processing options such as autocorrelation are available, the Fourier transform provides the most general and direct conversion between spatial (or temporal) domain and frequency domain. In practice, the fast Fourier transform (fFT) has been often used for these calculations because of its high computation efficiency. The fFT algorithm was developed to reduce both the time and cost of Fourier-transform numerical calculations used for the analysis of various periodic phenomena [7–11] and it was included in the "Top 10 Algorithms of the 20th Century" by IEEE (Institute of Electrical and Electronics Engineers), Computing in Science and Engineering [12]. The algorithm has been so popular that the limit of the frequency interval (i.e., resolution) imposed by the fFT method is often overlooked. The frequency interval [7,13,14], which is expressed as  $1/(N\Delta)$ , where  $N$  is the number of sampled data and  $\Delta$  is the sampled interval, provides the spectrum of phenomena in the frequency interval multiplied by an integer.

As an example, in the Talbot self-image analysis, the amount of data, the sampled interval, and the frequency interval are all determined by the measured images. To extract the dominant frequency information from the Talbot intensity modulation images, the fFT spectrum is often analyzed with a mathematical fitting method, such as the application of the center-of-mass algorithm to a grid of the frequency spectrum around the spectral peak and the fitting of the spectral peak with a parabolic or other mathematical model to precisely locate the spectral peak [15,16,20]. These fitting approaches have been successfully verified by various studies [16,17]. For some applications, these methods have been applied to distinguish a real peak signal in low signal-to-noise ratio (SNR) data [18]. Another interesting approach is the use of an interpolated input signal to enhance the precision of frequency analysis for data with few-kilohertz pulse repetition [19].

However, the output of those methods, depends strongly on the fitting conditions, such as the size of the grid, the location of the spectral peak in the fitting region, the background spectrum of the grid, and/or the number of fitting parameters. Thus, the application of a physically meaningful or well-established fitting model is critical for achieving a reliable result. As an extreme example, if a signal expected to exhibit a double-peak feature is fitted using a normal Gaussian model, the final outcome will be misleading.

Another common solution, known as the zero-padding approach, increases the array size of the original input image and the larger number of elements in the array improves the precision of the frequency analysis by providing a narrower frequency interval [7,13,14]. Unfortunately, the larger array size exponentially increases the calculation time. For instance, with the PC used in this work, the fFT time increased from 0.21 s to 1, 6, and 44 s for precisions of  $1/2$ ,  $1/2^2$ , and  $1/2^3$  of the original frequency interval (without zero padding), respectively. The rapidly increasing memory requirement for processing such a large number of elements is another critical factor that must be considered.

The fFT originated from the discrete Fourier transform; the two processes are often used interchangeably [21] for the study of frequency coordinates. However, the inherent frequency

interval limit of the fFT can be overcome using the discrete Fourier transform. Unfortunately, the discrete Fourier transform requires considerably longer computation time and processing resources.

Here, an iterative local Fourier transform (ilFT) method combining the fFT and the discrete Fourier transform along with a set of algorithms is presented. This iterative approach provides an attractive and practical solution to achieve both high computation efficiency and a good frequency resolution, as precise as  $2^{10}$  times higher than the fFT. Section 2 introduces the concept and processing algorithms of the ilFT by applying an iterative approach within a local frequency domain. The high efficiency, superb resolution, and overall performance of the method are systematically evaluated and compared with other high-resolution Fourier transform techniques in Section 3. Section 4 presents a demonstration of the ilFT for a Talbot self-image experiment that requires high-precision peak frequency determination. Section 5 summarizes the features of the new technique and its significance.

## 2. Algorithms for the ilFT

The discrete Fourier transform for two-dimensional sampled data  $g(x_i, y_j)$  that are a function of the spatial coordinate  $(x, y)$  can be expressed as [7,13,14]:

$$G(f_x, f_y) = \Delta^2 \sum_{i,j=1}^N g(x_i, y_j) e^{-j2\pi(f_x x_i + f_y y_j)}, \quad (1)$$

where  $(f_x, f_y)$  is the frequency coordinate used to calculate the spectrum and  $\Delta$  is the sampled interval (same in  $x$  and  $y$  direction). The spatial coordinates are expressed as the sampled interval multiplied by integers as follows:

$$x_i = i\Delta \text{ and } y_j = j\Delta. \quad (2)$$

In contrast to the fFT, which calculates the entire frequency spectral range at once, the discrete Fourier transform can only evaluate a set of arbitrarily or (if available) optimally selected frequency coordinates with a high resolution. The capability of the ilFT to achieve not only highly precise but also fast spectrum analysis is mainly based on strategically implementing this advantage.

Prior to a detailed discussion about each algorithm, it is important to acknowledge that the ilFT method does not extract super-resolution information, which is not originally contained in the raw data. In other words, the ilFT does not create or guess new information. Instead, it enables a powerful spectrum zoom-in feature to navigate existing and highly diverse information by using an efficient numerical process. The enhanced performance of the method mainly originates from its smart approach to avoiding practical limits, such as physical time, memory capacity, and other computing resources.

### 2.1 Searching for a dominant spectral peak

Figure 1 shows a schematic flow chart of the iterative process applied to determine a precise spatial frequency and period (e.g., Talbot self-image). This process uses an fFT computation to determine an initial spectral peak coordinate. Then,  $N \times M$  grid frequency coordinates around the spectral peak are formed with the coordinates sampled at  $1/2$  of the initial fFT frequency interval. A  $5 \times 5$  grid of frequency coordinates was used as an example case in Section 2. For each frequency coordinate location, Eq. (1) is utilized to calculate the frequency spectral value and a new spectral peak (with double precision) is searched among the  $N \times M$  spectral values. During the iterative process, the next  $N \times M$  grid frequency coordinates around the new peak are continually re-formed at  $1/2$  of the previous frequency interval. At every repetition, the frequency resolution is improved by factor of 2. For instance, ten iterations enhance the frequency precision by a factor of  $2^{10}$  compared to the initial

resolution. Although a frequency peak has been considered as the search target in this discussion, the target can be defined as any other spectral feature of interest.

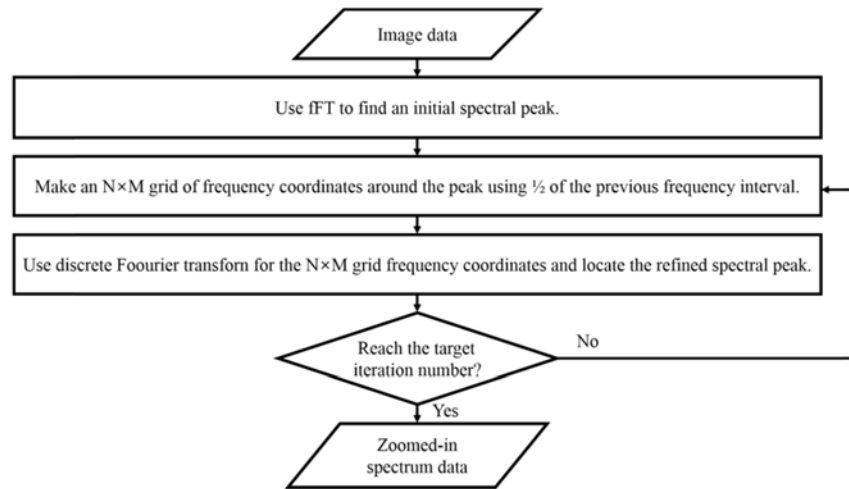


Fig. 1. Schematic flow chart showing the iterative spectrum zoom-in algorithm implemented in the iFFT method.

## 2.2 Three algorithms for high computing efficiency

Although the 250 ( $= 25$  coordinates  $\times 10$  iterations) computations required for the  $5 \times 5$  grid case of Section 2.1 are significantly less than the original  $1024^2$  spectral value calculations in the two-dimensional frequency coordinates, the 250 spectral values still require a long computation time owing to the heavy numerical load of the iFFT. As an example, each iFFT calculation for a frequency coordinate lasted approximately 0.18 s using a PC (CPU: i7-4550U with 1.50 GHz), whereas the fFT required approximately 0.21 s for the entire spectrum. (Note that these performance rates may depend on the specific computing environment, programming language, and other factors.) Considering the 250 (or more, as necessary) computations, it is essential to apply more efficient algorithms to reduce the calculation time while maintaining the high precision of the iFFT. Three algorithms were combined to improve the overall computing efficiency.

The first algorithm regularizes the number of elements used to calculate the spectrum during the iFFT iterations. For instance, in the results discussed in Section 4, the original image was zero padded to create a  $2048 \times 2048$  image that fulfills the condition of the image array size being equal to a power of 2, and approximately two thirds of the elements were zero. A sufficient (within an affordable calculation time for a given computing environment and tasks) zero padding in a regularized size produces a fast initial fFT result and, more importantly, a good initial estimation that guides the following iFFT iterations. However, the zero padding increases the integration domain of the iFFT. The integration range of the iFFT is limited only within the non-zero data area so that the iFFT calculations are not affected by the large regularized image size. For instance, this treatment reduced the computation time by approximately one third ( $= 3/8$ ) for the data processing discussed in Section 4.

The second algorithm recycles the previously calculated spectral values in the subsequent iteration steps by defining partly overlapping subsequent grid points. For instance, among the 25 coordinates of a  $5 \times 5$  grid considered in each repetition, the spectra of the nine coordinates are identical to the previous values because the nine grid points overlap with the previous locations, as depicted in Fig. 2. Instead of calculating for 25 new spectral values, this controlled zoom-in approach (enforcing identical locations) allows previous values to be recycled. On the other hand, if the 25 new locations are slightly differ from the previous

coordinates, no recycling is possible. For the  $5 \times 5$  grid case, the computing time is reduced by approximately one third ( $= 9/25$ ) with this approach. (Please, note that the second algorithm does not interpolate any values during the process. Instead, it calculates the exact new spectral values for the non-overlapping grid locations in the zoom-in area.)

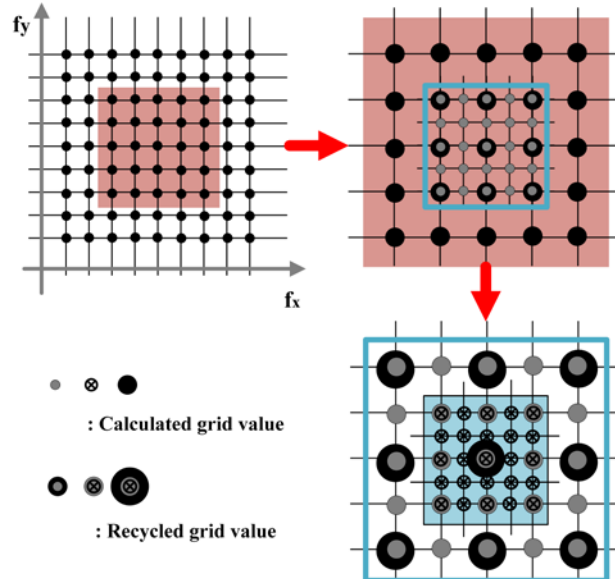


Fig. 2. Conceptual diagram depicting spectral value recycling during iFFT iterations.

The third algorithm adapts the next zoom-in coordinates with the assumption that the spectrum over the current grid area forms a pure convex shape. In other words, only a single spectral peak exists in the current searching range. When the iFFT evaluates a spectral value for a subsequent grid location, it examines the gradient of the newly evaluated spectral value and adapts the next evaluation grid point in situ. If the gradient is positive (i.e., indicating the approach to the peak), the opposite direction in the spectral domain is not investigated because it has a negative gradient. For a negative gradient case, the opposite direction in the spectral domain is examined. With this assumption, the number of necessary calculations to locate the peak can be further reduced. As the iFFT calculation time decreases almost proportionally to the number of evaluated spectral points, the total data processing time can be reduced by the third algorithm. The additional in situ searching process costs some computing resources but the gain from fewer iFFT calculations (with a 50% probability) is much more significant. The third algorithm can be disabled if too much noise exists near the peak or if the iFFT is utilized for a general spectrum zoom-in analysis, which is beyond single-peak detection and investigates fine details within a certain spectral range of interest (e.g., double-peak analysis, discussed in Section 3.3).

With the three algorithms, the overall data processing performance of the iFFT becomes highly efficient. For instance, the total time required for a spectral peak determination (for a  $1280 \times 1024$  pixels original image size) using ten iFFT iterations and the PC mentioned earlier in this section was measured to be  $\sim 1.8$  s. Although 1.8 s is longer than the 0.21 s needed for the FFT calculation, the final precision of the iFFT analysis was  $\sim 0.000092$  ( $= 1/(2048 \times 0.0052)/2^{10}$ )  $\text{mm}^{-1}$  compared to the frequency resolution of the FFT, which was  $\sim 0.094$  ( $= 1/(2048 \times 0.0052)$ )  $\text{mm}^{-1}$ .

### 3. Numerical performance analysis

The performance of the iFFT was evaluated and demonstrated using a series of numerical case-study simulations. In each case study, an ideal and mathematically defined input data set



was prepared, sampled, and processed using different Fourier transform methods in a common computing environment including computer, operating system, and programming language (i.e., MATLAB). Since the synthetic input data set represents the ideal signal, an algorithm's absolute performance can be objectively evaluated for various input data cases. Two widely used Fourier analysis methods were compared with the iFFT: a) a fFT with zero padding to control the final resolution [7,13,14] and b) an interpolated/fitting fFT method [14–17,20]. Various fields have successfully adopted these two approaches to analyze high-precision spectral data.

The total computing time was considered as the main performance figure of merit, as an indicator of the numerical efficiency of the method. A synthetic input wave was independently processed with the zero-padding fFT, the fitting fFT, and the iFFT to examine the reliability of the output frequency against the ideal input value, as shown in Fig. 3. For a visual demonstration and for simplicity, these case-study simulations were performed and are presented for  $N \times 1$  cases (i.e., vector cases), while a two-dimensional case using experimental data is presented in Section 4.

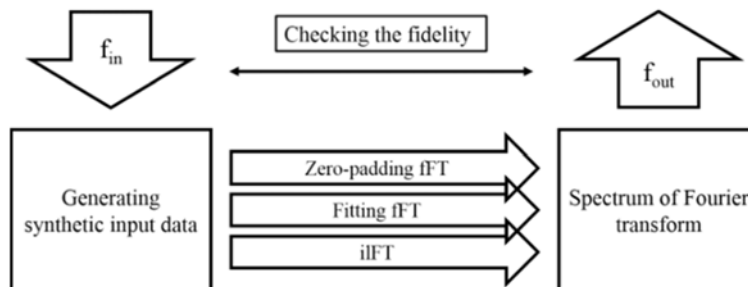


Fig. 3. Numerical case-study simulations comparing different Fourier analysis methods.

### 3.1 Case I: Computing efficiency comparison

The computing efficiency of the zero-padding fFT and the iFFT were evaluated and compared by measuring the computing time as a function of the final frequency resolution. The plot of the computing time as a function of resolution (Fig. 4) highlights the radically different trends of the two approaches.

The synthetic input sinusoidal signal was sufficiently sampled and fed to both a zero-padding fFT and an iFFT analyzer so that the output precision was not limited by the input signal sampling, but by each method's internal processing limits. The final frequency precision was defined as the resolution of the output spectrum map for this synthetic noise-free simulation study.

As shown in Fig. 4, the zero-padding fFT approach shows an exponentially increasing computing time as the necessary zero-padding area increases quickly to produce higher-resolution output. However, the iFFT exhibits an almost constant efficiency in the log-log plot as it continuously zooms into the spectral region of interest. For a relatively low target resolution (Zone-A in Fig. 4), the zero-padding fFT shows higher efficiency as the iFFT calculation in the iterative process requires more numerical computations. However, beyond a certain resolution point (Zone-B in Fig. 4), the iFFT provides higher efficiency. The resolution intersection point changes for a given computing environment but such a breakpoint should exist for every condition. The absolute slope of the efficiency plot may change for different hardware (e.g., faster CPU) but the relative trends remain the same.

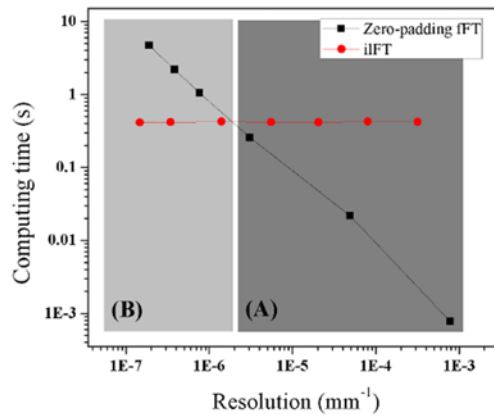


Fig. 4. Log-log plot comparing the computing efficiency between zero-padding FFT and iFFT.

The fitting FFT method was not included in this case study as such a fitting and interpolation approach can report any arbitrary resolution. However, with a suitable choice of fitting model, the fitting FFT may produce a meaningful high-precision result comparable to that of the iFFT. This topic is discussed in more detail in Section 3.3.

### 3.2 Case II: Precision comparison with a computing time constraint

The computing time and frequency resolution are often the most common trade-offs in spectrum analysis. For instance, a larger zero padding for FFT produces higher-precision frequency spectrum data at the expense of computing time and memory. The precision of the three different Fourier transform methods under the same time restriction ( $< \sim 0.1$  s) are compared in Fig. 5. (This case study was evaluated in Zone-B (Fig. 4) to provide a practical indication about the performance of the iFFT with a reasonable time limit and using modern computing resources.)

Below the  $\sim 0.1$  s processing time limit, the FFT could not afford sufficient zero-padding area to extract the fine frequency information of the varying input signal. The  $\pm 2\sigma$  deviation from the ideal input signal was  $\pm 5.08 \times 10^{-6} \text{ mm}^{-1}$ . In contrast, both the fitting FFT and the iFFT sufficiently extracted the exact frequency values of the input signal with  $\pm 2\sigma$  of  $\pm 1.84 \times 10^{-7} \text{ mm}^{-1}$  (for iFFT) and  $\pm 1.82 \times 10^{-7} \text{ mm}^{-1}$  (for fitting FFT). The superb precision performance (within a local spectral range of interest) of the iFFT and fitting FFT is thus demonstrated.

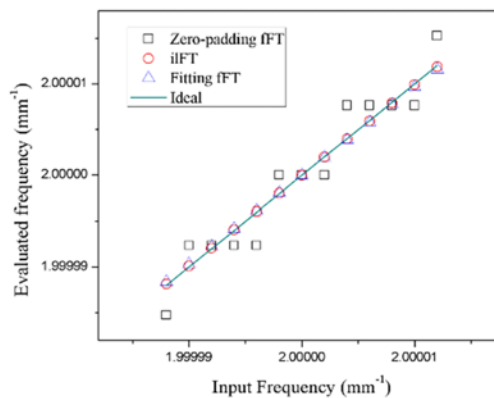


Fig. 5. Input frequency vs. evaluated frequency plot (with  $< \sim 0.1$  s processing time limit). The zero-padding FFT failed to trace the varying input frequency but the fitting FFT and the iFFT showed a good correlation between the input and evaluated values.

### 3.3. Case III: Zoom-in analysis for an unknown spectrum

Various fitting fFT methods have been successfully used as a high-precision analysis tool when a relevant fitting model is available. For instance, in Case I and Case II, a well-defined single-frequency output was expected and the fitting fFT method can provide a high-precision result. However, if the expected spectrum is unknown or no appropriate model exists, a pure zoom-in capability without the limitation of a pre-set model is highly desired.

A synthetic input signal containing two closely spaced frequency peaks was prepared and processed using the iFFT and fitting fFT with two basic polynomials (4th and 8th order). The performance comparison of the final spectrum outputs is presented in Fig. 6.

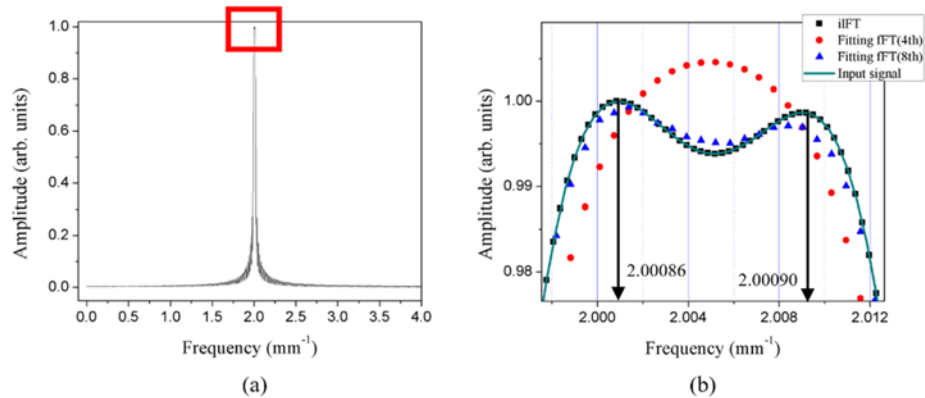


Fig. 6. Zero-padding FFT result showing the overall spectrum of the input data (a) and the zoom-in (red-box) spectrum comparing the iFFT and fitting fFT near the region of interest (b).

As shown in Fig. 6, the fitting fFT method using the 4th-order polynomial (red circles) cannot distinguish the double-peak input signal. Even when using the 8th-order polynomial (blue triangles), the fitted double-peak profile deviates from the ideal input signal (green solid line). The performance of the fitting fFT method can be improved if a more appropriate fitting model is applied. In contrast, the iFFT produced a high-fidelity result tracing the input signal with high resolution without any prior knowledge of the spectrum. Thus, the iFFT can be applied not only to a well-defined single frequency data case, but also to any complex frequency data cases such as aberrated fringes/images and multi-frequency signals. This demonstrates the powerful zoom-in capability of the iFFT to investigate a specific spectral region of interest.

## 4. Talbot self-image data analysis using the iFFT

The iFFT method was applied to process Talbot self-image experimental data, which require a precise spatial frequency analysis of the acquired fringe data [1–5]. Figures 7(a) and 7(b) show the experimental setup and a schematic diagram of the Talbot self-image configuration, respectively. A standard He-Ne laser ( $\lambda = 0.6328 \mu\text{m}$ ) with a  $5\text{-}\mu\text{m}$ -diameter pinhole was used to create a diverging point source. A translation stage was mounted with a  $0.05\text{-mm}$ -period grating (Edmund optics #58-777) and a CMOS (Complementary metal–oxide–semiconductor) detector (Mightex MCN) at a distance of approximately  $116 \text{ mm}$  from the pinhole. A micrometer with  $0.01 \text{ mm}$  resolution was attached to the translation stage.

The CMOS detector was located near the Talbot distance from the grating and the self-image of the grating was measured as a function of the distance between the pinhole and the grating/detector module. Each image acquired by the detector was stored in 8-bit depth (256 gray scale levels) at  $1024 \times 1280$  resolution. The detector pixel size was  $5.2 \times 5.2 \mu\text{m}$ . The gain and exposure time for the camera were adjusted so that the overall intensity of the image was below the saturation level. Each image was averaged after the acquisition of ten frames.



Figure 7(c) displays a  $512 \times 512$  section from the central area of a measured Talbot self-image.

The laser beam without the pinhole was used to align the detector and the grating. The microscope objective and pinhole were also aligned to generate a diverging beam with a uniform intensity over the detector area. The setup had no other optical elements (e.g., lens) that could cause optical wavefront aberrations. The low-spatial-frequency fringe pattern (on top of the regular vertical stripes) shown in Fig. 7(c) was attributed to the interference of multiple beams reflected from both sides of the grating glass substrate and from both sides of the protective cover glass in front of the detector. The off-axis concentric patterns indicate some residual misalignments.

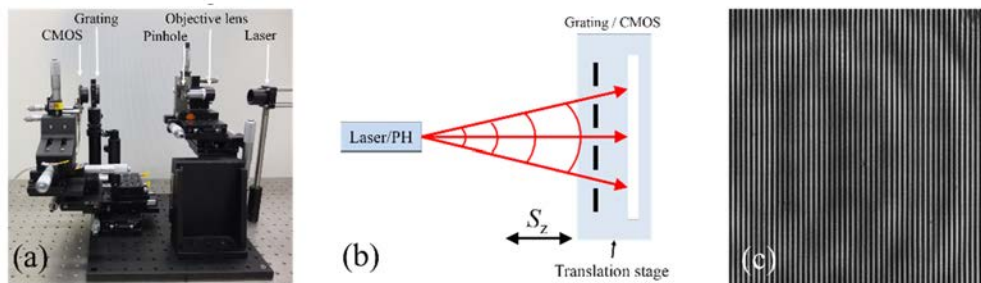


Fig. 7. (a) Talbot self-image experiment setup, (b) schematic layout (PH: pinhole,  $S_z$ : translation length), and (c) measured Talbot self-image.

Figure 7(c) shows  $\sim 50$  vertical stripes corresponding to a spatial frequency of  $\sim 19$  ( $= 1/(512 \times 0.0052/50)$ )  $\text{mm}^{-1}$ . Figure 8(a) presents the partial section of the frequency spectrum map processed by the FFT and a high-resolution zoom-in spectrum obtained by the iFFT is shown in Fig. 8(b). As shown in Fig. 8(b), the local frequency map provides a very fine resolution after ten iFFT iterations. For instance, with the standard MATLAB FFT, the spectral peak was detected at  $(18.87, 0)$   $\text{mm}^{-1}$ , which corresponds to a spatial period of 0.053 mm. In contrast, the iFFT method located the peak at  $(18.8732, 0.0059)$   $\text{mm}^{-1}$ , which corresponds to a period of 0.05299 mm. This high resolution also resolved the slight  $0.02^\circ$  rotation of the vertical stripes with respect to the vertical line of the detector.

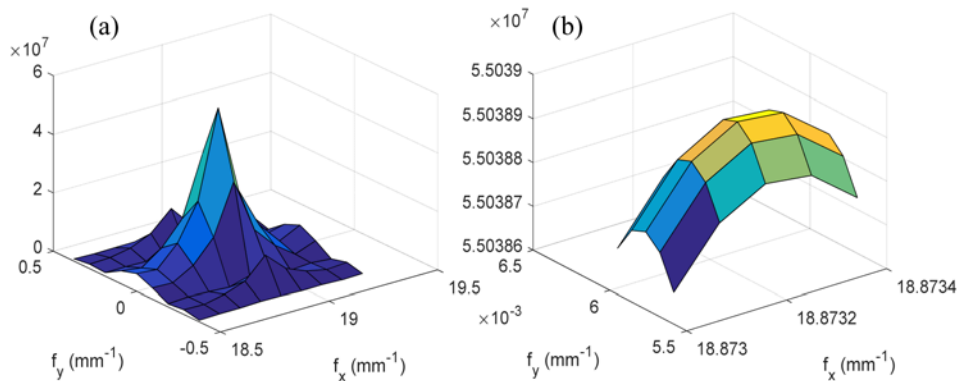


Fig. 8. Partial section of the frequency spectrum calculated by (a) the standard MATLAB FFT and (b) by iFFT for the Talbot self-image shown in Fig. 7(c).  $f_x$  and  $f_y$  represents the spatial frequency in x and y axis, respectively.

To confirm the reliability of the iFFT analysis, a set of Talbot self-images was measured and compared with the expected theoretical values. After a set of initial measurements, the pinhole-to-grating distance was varied up to 10 mm with an interval of 0.25 mm using the

micrometer attached to the mechanical stage. The grating-to-detector distance and the gain and exposure time of the camera remained fixed during the measurements. Each image was analyzed through the fFT and ilFT data processing pipelines.

Figure 9 shows the magnified (including demagnification) periods,  $p'$ , of the self-images processed by the ilFT and fFT as a function of translation length,  $S_z$  (shown in Fig. 7). The  $p'$  value for the Talbot self-image is theoretically expressed [22] as:

$$p' = p \left( 1 - \frac{d}{z} \right), \quad (3)$$

where  $p$  is the grating period,  $d$  is the grating-to-detector distance, and  $z$  is the pinhole-to-grating distance. The distance  $z$  changed with the change of the micrometer as follows:

$$z = z_0 + S_z, \quad (4)$$

where  $z_0$  is the unknown initial value for  $z$  ( $S_z = 0$ ) and  $S_z$  denotes the micrometer reading.

In practice, exact  $z_0$  and  $d$  measurements are often limited by the internal/external structures of the pinhole and detector. In addition, the magnified period depends nonlinearly on the variables,  $z_0$ ,  $d$ , and  $p$ . Therefore, instead of fitting the variables to a specified period (which, strictly speaking, contains some unknown uncertainties), the most-likely values were searched using the least sum of the squared differences between the measured and computed periods, which were calculated for each combination of variables ( $z_0$ ,  $d$ , and  $p$ ) over a set of ranges. The final (best) parameter values were  $z_0 = 116.56$  mm,  $d = 8.1820$  mm, and  $p = 500.00$   $\mu\text{m}$ . The black solid line in Fig. 9 represents the theoretical  $p'$  value obtained using these parameters and Eq. (3).

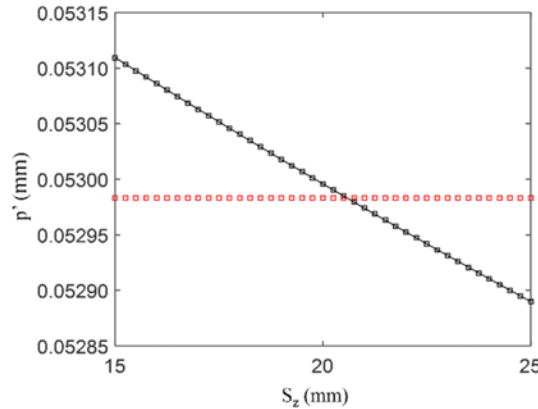


Fig. 9. Magnified period  $p'$  of the measured Talbot self-images as a function of pinhole-to-grating distance, denoted by the micrometer reading  $S_z$ . The red squares represent the fFT result and the black squares the ilFT result. The black solid line corresponds to the expected theoretical model.

The black square symbols in Fig. 9 show that the ilFT results have an excellent agreement with the expected theoretical values (black solid line) as a function of  $S_z$ . The decreasing  $p'$  trend exhibited by both the experimental data and the corresponding theoretical prediction suggests that the ilFT can be utilized to determine a frequency or the corresponding period as precisely as anticipated. In contrast, the results of the fFT analysis (red squares in Fig. 9) suffer from insufficient precision in detecting the small variations of  $p'$ . In other words, the fFT-processed  $p'$  values did not change in the 41 images.

The frequency resolution of the fFT,  $0.094 \text{ mm}^{-1}$ , can be considered as the frequency uncertainty,  $\Delta f$ . The corresponding uncertainty for the period measurement,  $\Delta p'$ , can be expressed as:

$$|\Delta p'| = p'^2 \Delta f. \quad (5)$$

Therefore,  $\Delta p' \approx 0.00026$  mm when  $p'$  is equal to the average value of 0.053 mm. To demonstrate the relative resolution advantage of the ilFT, a 10-mm  $S_z$  range was selected after a number of trials to limit the expected variation of the magnified period to below  $\Delta p'/2$ . Figure 9 shows that the total variation was approximately  $\pm 0.00011$  mm. Therefore, the period values in the examined range varied so little that they could not be resolved by the fFT. (This does not represent a fundamental limit of the fFT method. With sufficient computing resources allowing sufficient zero padding, fFT could also produce similar results, as discussed in Section 3.) This experimental result successfully demonstrates the attractive advantages of the ilFT, which allows simultaneously efficient and precise spectrum analysis.

## 5. Concluding remarks

The ilFT method, which implements a set of new algorithms combined with the optimal use of the discrete Fourier transform, has been developed for a precise frequency peak determination and/or zoom-in spectrum investigation. Based on systematic case-study simulations presented in Section 3 and the Talbot self-image analysis detailed in Section 4, the high computing efficiency and superb precision of the ilFT have been successfully demonstrated and confirmed. For instance, an improvement by a factor of  $2^{10}$  compared to the frequency resolution of standard fFT was achieved in a few seconds of processing time. A set of measurements of the magnified period of Talbot self-images was analyzed using the ilFT method and a good agreement between the experimental data and the theoretical model was confirmed. The ilFT method can be applied to various types of spectral analysis (e.g., interferogram conditioning and phase retrieval in optical metrology [23]) that require both calculation efficiency and high-precision capability within the spectral range of interest.

## Acknowledgments

This study was supported by Inha University and the College of Optical Sciences, University of Arizona. Also, this material is based in part upon the data processing software development supported by the II-VI Foundation Block grant.